

# The Peculiar Electronic Structure of PbSe Quantum Dots

J. M. An,\* A. Franceschetti, S. V. Dudy, and Alex Zunger\*

National Renewable Energy Laboratory, Golden, Colorado 80228

Received July 20, 2006

## ABSTRACT

PbSe is a pseudo-II-VI material distinguished from ordinary II-VI's (e.g., CdSe, ZnSe) by having both its valence band maximum (VBM) and its conduction band minimum (CBM) located at the fourfold-degenerate L-point in the Brillouin zone. It turns out that this feature dramatically affects the properties of the nanosystem. We have calculated the electronic and optical properties of PbSe quantum dots using an atomistic pseudopotential method, finding that the electronic structure is different from that of ordinary II-VI's and, at the same time, is more subtle than what k·p or tight-binding calculations have suggested previously for PbSe. We find the following in PbSe dots: (i) The intraband (valence-to-valence and conduction-to-conduction) as well as interband (valence-to-conduction) excitations involve the massively split L-manifold states. (ii) In contrast to previous suggestions that the spacings between valence band levels will equal those between conduction band levels (because the corresponding effective-masses  $m_e \approx m_h$  are similar), we find a densely spaced hole manifold and much sparser electron manifold. This finding reflects the existence of a few valence band maxima in bulk PbSe within  $\sim 500$  meV. This result reverses previous expectations of slow hole cooling in PbSe dots. (iii) The calculated optical absorption spectrum reproduces the measured absorption peak that had previously been attributed to the *forbidden*  $1S_h \rightarrow 1P_e$  or  $1P_h \rightarrow 1S_e$  transitions on the basis of k·p calculations. However, we find that this transition corresponds to an allowed  $1P_h \rightarrow 1P_e$  excitation arising mainly from bulk states near the L valleys on the  $\Gamma$ -L lines of the Brillouin zone. We discuss this reinterpretation of numerous experimental results.

Rocksalt-structured PbSe<sup>1</sup> quantum dots have emerged recently as interesting quantum systems,<sup>2–16</sup> following the long dominance of CdSe as the paradigm colloidal nanostructure. The “pseudo II-VI” compound<sup>1</sup> PbSe is indeed a unique material, compared to II-VI metal monoselenides (ZnSe, CdSe, etc.). Because of the high atomic number of the Pb cation, relativistic effects<sup>1</sup> localize its valence 6s orbital, making this orbital chemically inactive and transforming this s<sup>2</sup>p<sup>2</sup> column-IV element into a pseudo-divalent p<sup>2</sup> atom. Lead thus forms metal *monoselenides* just like the column-II s<sup>2</sup> Zn or Cd atoms do. Moreover, the relativistic lowering of the Pb 6s orbital energy pulls down the normally empty cation s conduction band  $L_6^+ - \Gamma_6^+ - X_6^+$  into the occupied *valence* band manifold. Inside the valence band, this new band (located 6–8 eV below the HOMO) finds a higher-lying  $L_{6v}^+$  state of the same point group symmetry; the anticrossing repulsion between these equal symmetry states then makes the upper  $L_{6v}^+$  state the valence band maximum<sup>1</sup> (VBM). Similarly, the lowest empty  $L_{6c}^-$  state is repulsed downward by higher-energy conduction L states of the same symmetry, thus making the conduction band minimum (CBM) L-like also. Hence, PbSe has a unique electronic structure, whereby both the VBM and the CBM are L-like states. This unusual feature of bulk PbSe<sup>17</sup> leads to unique properties of PbSe quantum dots that distinguish

them from CdSe dots. We wish to address three pertinent questions here:

(i) *What are the mechanisms and degree of L-levels splitting in the PbSe dot?* Because in the fcc Brillouin zone there are four equivalent L-point valleys, the VBM and CBM states of bulk PbSe are fourfold degenerate (eightfold degenerate including spin). However, because of the removal of translational symmetry in the dots, there will be (a) intervalley coupling that will split the bulk-degenerate L states,<sup>18</sup> and (b) valence-conduction interband coupling that will further modify these L states. Furthermore, (c) the strong anisotropy of the bulk L valleys in PbSe, with transverse (t) and longitudinal (l) effective masses<sup>19</sup> being rather different ( $m_t/m_l$  being 1.75 for electrons and 2.0 for holes at 4 K), will further split the near-edge quantum dot states. Finally, (d) the magnitude of the potential barrier surrounding the dot will decide the spacings between these split L levels.

Attempts to theoretically account for all four L-splitting effects (a–d) in PbSe dots have proven difficult. The  $4 \times 4$  L-centered<sup>20</sup> k·p approach recently proposed in the literature<sup>5,12,13</sup> ignores intervalley coupling (a), limits the valence-conduction coupling (b) to a single (doubly degenerate) band for each edge, and either neglects<sup>11</sup> or incorporates<sup>5,12,13</sup> the L-valley anisotropy effect (c), albeit within the effective-mass approximation. This k·p approximation<sup>5,11–13</sup> was applied using an infinite potential barrier, thus preventing the carrier wavefunctions from delocalizing outside the dot

\* Corresponding authors. E-mail: joonhee\_an@nrel.gov; alex\_zunger@nrel.gov.

and therefore exaggerating the degree of quantum confinement (d). Tight-binding calculations<sup>14,15</sup> incorporate in principle all four effects (a–d). However, the tight-binding fit<sup>14</sup> to the bulk band structure of PbSe had missed most of the L-valley anisotropy:  $m_l/m_t = 0.0374/0.0462 = 0.81$  was used for electrons instead of the experimental  $0.070/0.040 = 1.75$  (see ref 19) and  $0.0468/0.0472 = 0.99$  was used for holes instead of the experimental  $0.068/0.034 = 2.0$ . Consequently, effect (c) was improperly accounted for. We conclude that the splittings of L states in PbSe dots have not been properly understood or predicted, and thus the near-edge absorption spectra of the dots remain unexplained. We will show that a proper inclusion of effects (a)–(d) correctly reproduces both the intraband and the interband absorptions of PbSe dots.

(ii) *What is the origin of the observed interband absorption peaks?* Experimentally, it is possible to resolve three peaks in the absorption spectrum of ensembles of PbSe nanocrystals.<sup>3,4,6,8,11,15,16</sup> On the basis of the coincidence between the measured and  $k \cdot p$  calculated transition energies, it was suggested<sup>11</sup> that the three observed peaks originate from  $S_h \rightarrow S_e$ ,  $S_h \rightarrow P_e$  (or  $P_h \rightarrow S_e$ ) and  $P_h \rightarrow P_e$  transitions, respectively. This assignment was later confirmed by tight-binding (TB) calculations.<sup>14</sup> Thus, in this interpretation,<sup>11,14</sup> the second observed absorption peak corresponds to formally forbidden optical transitions  $P \rightarrow S$  and  $S \rightarrow P$ , which violate the parity conservation rule. This assignment has prompted widespread speculations<sup>3,7,8,11,14,15</sup> as to the mechanism responsible for making this nominally forbidden absorption peak strongly allowed. However, both  $k \cdot p$  and TB calculations upon which this assignment was made have deficiencies. The  $k \cdot p$  calculations were based on a  $4 \times 4$  isotropic model with an infinite confinement barrier. Such a model ignores the existence of additional valleys, both in the valence and conduction bands, which can contribute to the absorption spectrum. The large confinement barrier used in  $k \cdot p$  calculations certainly exaggerates the extent of quantum confinement, hence placing the  $S$ – $P$  transition at too high an energy; its agreement with experiment is thus spurious. This is apparent from Figure 1 contrasting the  $k \cdot p$  eigenvalue ladder of a  $30.6 \text{ \AA}$  dot (copied digitally from Figure 1c of ref 11) with our atomistic calculation (see below). Clearly,  $k \cdot p$  misses altogether numerous valence eigenvalues in the top 500 meV range below the valence band maximum (VBM), having spuriously shifted them to much deeper energies, on account of the artificially large  $k \cdot p$  confinement effects. The overestimation of confinement in such  $4 \times 4$   $k \cdot p$  calculations<sup>11</sup> is also evident from the fact that its confined levels scale with the dot size,  $d$ , as  $1/d^2$ , whereas more realistic multiband calculations with finite barriers<sup>14</sup> show a much weaker confinement with  $1/d$  scaling. The TB calculations,<sup>14</sup> however, used a parametrization that was fit to incorrect electron and hole effective masses, as noted above.

Recently, using a combination of optical spectroscopy and electron- and hole-tunneling spectroscopy, Liljeroth et al.<sup>15</sup> have proposed that the second absorption peak corresponds to the  $P_h \rightarrow P_e$  transition (which is optically allowed),

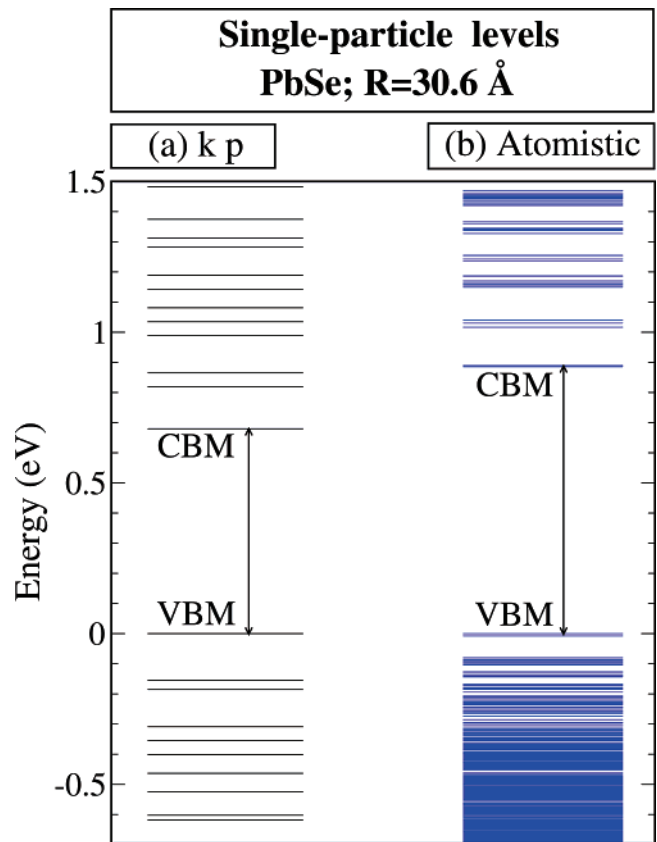


**Figure 1.** Single-particle energy levels for  $R = 30.6 \text{ \AA}$  PbSe dot calculated using (a) the  $k \cdot p$  method<sup>11</sup> (copied digitally from ref 11) and (b) the pseudopotential method. The valence band maximum (VBM) energies are aligned.

whereas the third absorption peak corresponds to the  $D_h \rightarrow D_e$  transition. The debate on whether the cross transitions such as  $S_h \rightarrow P_e$  are strong<sup>5,8,11</sup> or weak<sup>15</sup> is important to the understanding of carrier dynamics: Ellingson et al.<sup>11</sup> have recently argued that because asymmetric transitions such as  $P_h \rightarrow S_e$  are expected to lead to strong exciton–phonon coupling, they would allow rapid relaxation of excited carriers via electron–phonon coupling. We will show here that  $P_h \rightarrow S_e$  and  $S_h \rightarrow P_e$  transitions are indeed forbidden, and that the second transition is a  $P_h \rightarrow P_e$  transition (in agreement with Liljeroth et al.<sup>15</sup>) that originates from  $L_{||}$  bands (i.e., states along the  $\Gamma$ – $L$  line) and does not have a pure single-band assignment in terms of being “ $P_h$ ”. The third transition is not a pure  $D_h \rightarrow D_e$  excitation<sup>15</sup> but is made up of heavily mixed  $P_h \rightarrow P_e$  and  $D_h \rightarrow D_e$  transitions.

(iii) *Are the spacings between hole levels equal to the spacings between electron levels?* If one assumes an infinite potential well with  $m_e \approx m_h$  as in the  $k \cdot p$  calculations,<sup>11</sup> then the hole-level spacings must equal the electron-level spacings. This assumption has played a central role in the contemporary literature<sup>2,5,6,8,10,11,16</sup> on PbSe quantum dots. For example, Klimov et al.<sup>10,16,21</sup> used this assumption, together with the forbidden character of the cross transitions (e.g.,  $P_h \rightarrow S_e$ ), to argue that the threshold for carrier multiplication in PbSe quantum dots is  $3E_g$ , where  $E_g$  is the quantum dot band gap. Schaller et al.<sup>16</sup> used the assumption of equal electron- and hole-level spacings to conclude that Auger-

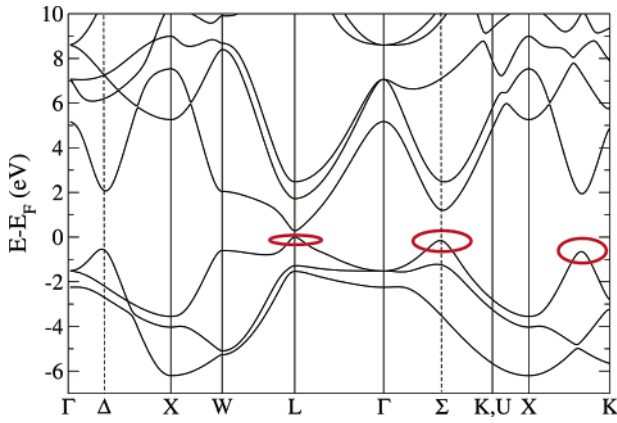


**Figure 2.** EPM band structure of bulk PbSe, where the zero of energy is the top of the valence band, and three valence band maxima within the first 500 meV below the zero energy are highlighted with red ellipses. The existence of the three valence band maxima is confirmed by the bulk band structure reported in ref 19.

assisted electron cooling should be slow, and thus other scattering mechanisms are required to explain the observed picosecond electron cooling rate. As shall be shown below, an atomistic calculation of the energy levels of PbSe dots indicates that hole states are much more dense than electron states (viz. Figure 1) because hole states arise not only from L points but also from  $\Sigma$  points (viz. Figure 2). The atomistic calculation thus invalidates previous expectations of electron–hole mirror symmetry and the presumed far-reaching consequences<sup>10,16,21</sup> of such an effect.

Our work is aimed at understanding the three puzzles (i–iii) noted above.

**Method of Calculation.** We study here two dots, Pb<sub>260</sub>Se<sub>249</sub> and Pb<sub>2046</sub>Se<sub>2117</sub>. We construct PbSe dots having the rocksalt structure (lattice constant  $a = 6.117$  Å) by placing a Se atom at the center of a sphere with an effective radius,  $R$ , and then adding Pb or Se atoms within  $R$  according to the structure. For such large dots, the electronic properties do not change much if we place a Pb atom at the dot center. The effective radius,  $R$ , is calculated using the formula  $R = a(\gamma N_{\text{dot}})^{1/3}$ , where  $\gamma = 3/32\pi$  and  $N_{\text{dot}}$  is the total number of real atoms in a dot. The two dots considered here have  $R = 15.3$  Å and  $R = 30.6$  Å (16.7 Å and 31.9 Å, including passivation), respectively.

The eigenenergies and eigenfunctions of the quantum dots are obtained by solving an effective Schrödinger equation

$$\left[-\frac{1}{2}\nabla^2 + V(\mathbf{r}) + V_{\text{SO}}\right]\psi_i(\mathbf{r}) = E_i \psi_i(\mathbf{r}) \quad (1)$$

where the wavefunctions,  $\psi_i(\mathbf{r})$ , are expanded in a plane wave basis set, and  $V_{\text{SO}}$  is a spin–orbit term. The local potential,  $V(\mathbf{r})$ , is represented as a superposition of screened atomic pseudopotentials<sup>22</sup> for atom species  $\alpha$  at site  $\mathbf{d}_\alpha$  in cell  $\mathbf{R}$

$$V(\mathbf{r}) = \sum_{\alpha} \sum_{\mathbf{R}} v_{\alpha}(|\mathbf{r} - \mathbf{R} - \mathbf{d}_{\alpha}|) \quad (2)$$

**Table 1.** Comparison of PbSe of Band Energies (in eV), Band Gap  $E_g$  (in eV), and Effective Masses (in Units of Electron Mass) as Obtained in Our Screened Pseudopotential Approach and Experiments ( $\Omega$  is the Unit Cell Volume)

property	target value	fitted value	property	target value	fitted value
$E_g(\text{L})$	0.278 <sup>a</sup>	0.28	$L_{45c}^- - L_{6v}^+$	1.75 <sup>a</sup>	1.72
$\Gamma_{8v}^-$	5.5	5.52	$L_{6c}^- - L_{45v}^+$	1.53 <sup>a</sup>	1.56
$\Gamma_{6c}^-$	5.2 <sup>b</sup>	6.69	$\Delta(\Gamma)$	0.75 <sup>c</sup>	0.73
$\Gamma_{6v}^+$	-4.8 <sup>c</sup>	-7.35	$\Delta(\text{L})$	0.25 <sup>d</sup>	0.25
$L_{45v}^+$	1.45 <sup>c</sup>	1.52	$\Delta(\text{X})$	0.6 <sup>c</sup>	0.48
$L_{6v}^+$	-7.24 <sup>b</sup>	-9.82	$m_{lc}(\text{L})$	0.07 <sup>a</sup>	0.07
$X_{7c}^+$	5.6 <sup>b</sup>	6.78	$m_{tc}(\text{L})$	0.04 <sup>a</sup>	0.04
$X_{6v}^-$	-1.3 <sup>c</sup>	-2.52	$m_{lv}(\text{L})$	0.068 <sup>a</sup>	0.07
$X_{6v}^-$	-3.0 <sup>c</sup>	-4.69	$m_{6c}(\text{L})$	0.034 <sup>a</sup>	0.04
$L_{45c}^-$	3.1 <sup>b</sup>	3.99	$-\Omega(dE_g/d\Omega)$	4.9 <sup>e</sup>	4.97
$L_{6c}^-$	1.728	1.80			

<sup>a</sup> Reference 19. <sup>b</sup> Reference 33. <sup>c</sup> Reference 34. <sup>d</sup> Reference 35. <sup>e</sup> Calculated with experimental pressure coefficient and bulk modulus in ref 19.

The individual screened spherical atomic potentials,  $v_{\alpha}$ , and the spin–orbit potential,  $V_{\text{SO}}$ , have been fitted in such a way that solving eq 1 for the *bulk* solid reproduces the measured band structure, deformation potential, effective mass, and spin–orbit splittings of PbSe, as listed in Table 1. The form<sup>22,23</sup> of the atomic potentials is

$$v_{\alpha}(\mathbf{q}) = a_0 \frac{\mathbf{q}^2 - a_1}{a_2 e^{a_3 q^2} - 1} \quad (3)$$

where  $a_0$ ,  $a_1$ ,  $a_2$ , and  $a_3$  are the fitting parameters for each atom type  $\alpha$  ( $a_0 = 0.224$ ,  $a_1 = 2.889$ ,  $a_2 = 1.571$ , and  $a_3 = 0.378$  for Pb and  $a_0 = 23.951$ ,  $a_1 = 3.053$ ,  $a_2 = 58.437$ , and  $a_3 = 0.666$  for Se, all in atomic units). The band structure of bulk PbSe calculated using the fitted potentials is shown in Figure 2. The fit is done for low temperature, except that the bulk band gap,  $E_g$ , is fitted to room-temperature experiments. The pseudopotential ratio between longitudinal and transverse effective masses for electrons is  $m_l/m_t = 0.066/0.035 = 1.886$  and for holes  $0.072/0.038 = 1.895$ , in good agreement with experiment.<sup>19</sup> The dangling bonds at the surface of the quantum dots are passivated by “ligand potentials” of a Gaussian form  $u_{\alpha} = u_{\alpha}^0 \exp(-(0.75|\mathbf{q}|)^2)$  ( $u_{\alpha}^0 = 12$  hartrees for cation-site passivation and  $u_{\alpha}^0 = -7.2$  hartrees for anion-site passivation) in order to remove all surface states<sup>22</sup> from the dot band gap to  $\sim 1$  eV away from the band edges. Calculations with imperfect passivation such as those done by us for CdSe dots<sup>24</sup> have not been done for PbSe dots.

To solve eq 1, we have used the folded spectrum method.<sup>25</sup> To analyze the results, we have subjected all wavefunctions to a “majority representation” decomposition<sup>26</sup>  $\psi_i(\mathbf{r}) = \sum_{\mathbf{k}} A_i(\mathbf{k}) e^{i\mathbf{k}\cdot\mathbf{r}}$ , which identifies the dominant wavevectors contributing to each dot state. To address the anisotropic nature of dot wavefunctions, we integrate  $\hat{\mathbf{k}}|A_i(\mathbf{k})|^2$  over a quarter-hemisphere cornered at each L point and then sum  $\int \hat{\mathbf{k}}|A_i(\mathbf{k})|^2 d^3k$  over all available L points.

We have calculated the intraband and interband absorption spectra. Because the dielectric constant of PbSe is quite large ( $\epsilon_\infty = 23$ ,  $\epsilon_0 = 250$ ), carrier–carrier interactions are highly screened, so we can calculate the absorption spectra in the single-particle (SP) approximation

$$I_{\text{sp}}(\omega) = \frac{1}{V} \sum_{v,c} |\mathbf{M}_{v,c}|^2 \delta(\hbar\omega - E_c - E_v) \quad (4)$$

where  $V$  is the volume of the supercell encaging the quantum dot, and the sum runs over all pairs of valence ( $v$ ) and conduction ( $c$ ) states. Here,  $\mathbf{M}_{v,c}$  is obtained using the dipole approximation, that is,  $\mathbf{M}_{v,c} = \langle \psi_v | \mathbf{r} | \psi_c \rangle$ .

**Single-Particle Spectrum.** Figure 1 shows the single-particle energy levels calculated using our atomistic pseudopotential method, compared with the  $\mathbf{k}\cdot\mathbf{p}$  calculations of ref 11. We see from Figure 1 that (a) the  $\mathbf{k}\cdot\mathbf{p}$  band gap<sup>11</sup> is smaller (despite a larger confinement), presumably due to the fit done in ref 11 to their uncharacteristically small measured band gaps.<sup>27</sup> (b) The atomistically calculated valence energy levels are far more closely spaced than in  $\mathbf{k}\cdot\mathbf{p}$  because in the latter approach intervalley coupling, effective-mass anisotropy, and finite barrier confinement are neglected. The reason that the hole levels in the first  $\sim 500$  meV below the VBM are much more dense than the electron levels is that in bulk<sup>1</sup> PbSe there are three valence band maxima (see Figure 2) within the first 500 meV: (i) L, (ii) between L and K on the  $\Sigma$  line, and (iii) between K and X. These bulk dispersion maxima fold into the center of the Brillouin zone for the dot. In contrast, the conduction band has only one conduction band extremum within the first 500 meV above the CBM. (c) The proposed<sup>5,10,11,16,21</sup> “mirror symmetry” between conduction and valence states (by which  $E_{\text{CBM}+n} - E_{\text{CBM}} = E_{\text{VBM}+n} - E_{\text{VBM}}$ ) does not exist in the atomistic calculation and is an artifact of simplified model assumptions.

The assumed mirror-like symmetry between valence and conduction levels has often been used to interpret experimental results as follows:

(i) Wehrenberg et al.<sup>4</sup> found similar energies for the first valence–valence and conduction–conduction intraband absorption peaks. They interpreted these peaks as arising from  $1S_h \rightarrow 1P_h$  and  $1S_e \rightarrow 1P_e$  transitions, which would have the same energy, if mirror symmetry is assumed. However, we will see in Section III that our atomistic calculation reproduces these intraband spectra well, without the need to assume such a symmetry.

(ii) The relatively fast intraband relaxation rate<sup>3,8,16</sup> of 3–6 ps in PbSe quantum dots has been explained by a polaron model,<sup>16</sup> assuming that the mirror-like symmetry precludes the possibility of Auger-type electron–hole energy transfer. However, our calculated dense valence energy levels do allow for efficient hole cooling, suggesting that the Auger-type energy transfer cannot be ruled out as the source of electron cooling.

(iii) The recent observation<sup>10</sup> of efficient carrier multiplication for  $\hbar\omega > 3E_g$  has also been interpreted as a confirmation of the mirror-like symmetry between valence and conduction

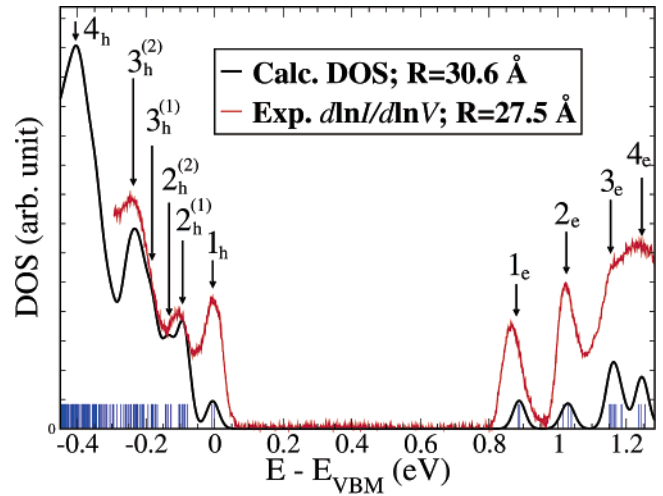


**Figure 3.** Density of states (black solid curve) of the  $R = 30.6$  Å dot calculated by broadening each single-particle energy level (blue solid bars) by 25 meV Gaussian, and measured  $d \ln I / d \ln V$  (red solid curve) of the  $R = 27.5$  Å dot from ref 15 except that  $\eta = (V_{\text{dot}} - V_{\text{tip}}) / V_{\text{bias}} = 0.75$  instead of  $\eta = 0.70$  (P. Liljeroth, private communication). The electron (hole) peaks are numbered in order of increasing (decreasing) energy, along with the subscripts “e” (“h”).

energy levels. However, the threshold of  $\hbar\omega_{\text{th}} = 3E_g$  simply reflects the mirror-like symmetry of *high-lying states* in both conduction and valence bands, that is, conduction states near  $E_{\text{CBM}} + E_g$  and valence states near  $E_{\text{VBM}} - E_g$ . In other words, the high-energy impact ionization threshold does not necessarily imply a mirror-like symmetry of the lower-lying states involved in the near-gap optical absorption spectra because their energies are much smaller than the extra energy,  $E_g$ , required for carrier multiplication. Ellingson et al.<sup>11</sup> reported a different threshold of  $\hbar\omega_{\text{th}} = 2.1 E_g$ , by assuming that parity-forbidden asymmetric transitions such as  $P_h \rightarrow S_e$  or  $S_h \rightarrow P_e$  are in fact optically allowed within the mirror-like symmetry scenario. We have found<sup>28</sup> instead that the  $2.1 E_g$  threshold is due to the lack of mirror-like symmetry, not to optically forbidden transitions. In other words, the asymmetry between the valence-band and conduction-band densities of states allows for optical transitions where the excess energy of the electron is significantly larger than that of the hole.

**Comparison of Single-Particle States with Tunneling Spectroscopy.** The calculated spacings between the electron density of states (DOS) peaks (and, separately, the hole DOS peaks) can be compared with tunneling spectroscopy measurements,<sup>15</sup> if we assume that quasi-particle polarization self-energies are similar for different electron states.<sup>29</sup> The black solid curve in Figure 3 shows the calculated single-particle DOS for  $R = 30.6$  Å, using a Gaussian broadening of 25 meV, and the red curve shows the measured tunneling spectrum<sup>15</sup>  $d \ln I / d \ln V$  for  $R = 27.5$  Å. The calculated degeneracy splitting between the lowest four S-like levels is  $\sim 15$  meV for holes and  $\sim 5$  meV, due to the intervalley coupling. The agreement between our results and experiment is excellent, as summarized in Figure 3 and Table 2. This indicates that the calculated single-particle energy levels are

**Table 2.** Peak-to-Peak Energy Separations in eV Extracted from Tunneling Spectra<sup>15</sup> in Comparison with the Peak-to-Peak Separations from the Calculated DOS (Figure 3)

radius (Å)	$1_h-2_h^{(1)}$	$1_h-3_h^{(2)}$	$2_h^{(1)}-3_h^{(2)}$	$3_h^{(2)}-4_h$	$1_e-2_e$	$1_e-3_e$	$2_e-3_e$	$3_e-4_e$
21.5 <sup>a</sup>	0.135	0.232	0.097	0.134	0.140	0.256	0.116	0.080
15.3 <sup>b</sup>	0.140	0.268	0.128	0.152	0.281	0.368	0.087	0.074
27.5 <sup>a</sup>	0.095	0.224	0.129		0.145	0.272	0.127	0.056
30.6 <sup>b</sup>	0.090	0.227	0.137	0.119	0.144	0.278	0.134	0.080

<sup>a</sup> Tunneling measurements, ref 15. <sup>b</sup> Presently calculated values.

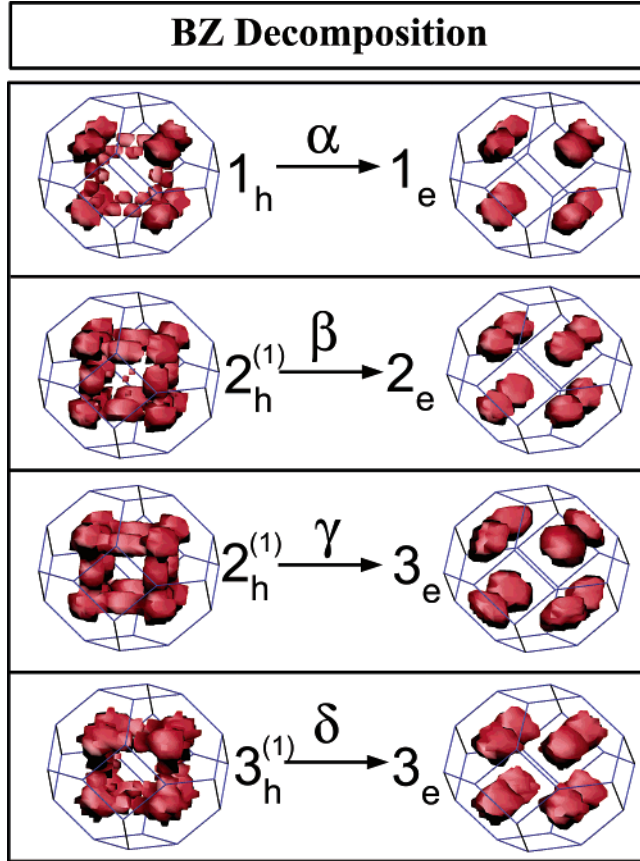


**Figure 4.** Projection of some dot wavefunctions representative of the interband transitions,  $\alpha$ ,  $\beta$ ,  $\gamma$  and  $\delta$ , for  $R = 30.6 \text{ \AA}$ : red iso-surfaces stand for mean values of  $|A_i(\mathbf{k})|^2$  in the first BZ of the fcc lattice.

accurate enough to describe other properties, for example, optical spectra, of the PbSe quantum dots.

Figure 4 shows the majority representation of the numbered DOS peaks of Figure 3, and Table 3 shows the quantitative analysis of their majority representation and L-point anisotropy. These DOS peaks show two types of state mixing: (i) L- $\Sigma$  mixing: while the band-edge states,  $1_h$  and  $1_e$ , derive from the L valleys alone, this is not the case for deeper hole states that spread toward different L valleys (viz. Figure 4), producing some  $\Sigma$  character. For instance, peak  $2_h^{(1)}$  is made up of two types of states, [a] and [b], and contains noticeable  $\Sigma$  character: type [a] has 20 %  $\Sigma$  character, and type [b] has 80 %  $\Sigma$  character. (ii)  $L_{||}$ - $L_{\perp}$  mixing: the anisotropic nature of the L states splits the levels into  $L_{||}$  and  $L_{\perp}$  components. Valence states having higher  $L_{\perp}$  character tend to be farther from the band edges because of their smaller transverse effective mass.

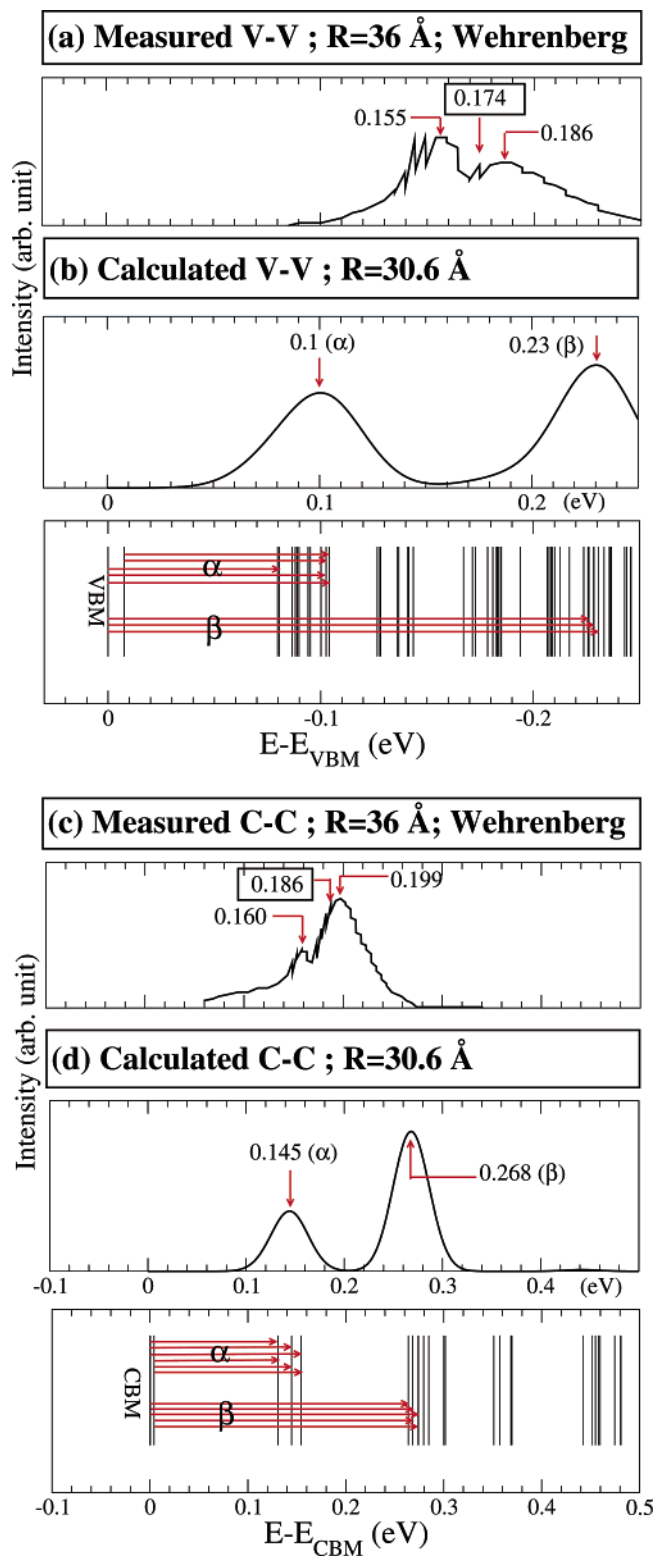
**Table 3.** Majority Representation Characters (see Figure 4) of the DOS Peaks Shown in Figure 3<sup>a</sup>

peak	character
$1_h$	$1.0[0.9L_{  } + 0.1L_{\perp}]$
$2_h^{(1)}$	[a] $0.8[0.9L_{  } + 0.1L_{\perp}] + 0.2\Sigma$ ; [b] $0.1L_{  } + 0.8\Sigma$
$2_h^{(2)}$	$0.3L_{  } + 0.5\Sigma$
$3_h^{(1)}$	[a] $0.9[0.9L_{  } + 0.1L_{\perp}]$ ; [b] $0.6[0.7L_{  } + 0.3L_{\perp}] + 0.2\Sigma$
$3_h^{(2)}$	[a] $0.9[0.4L_{  } + 0.6L_{\perp}] + 0.1\Sigma$ ; [b] $0.9[0.7L_{  } + 0.3L_{\perp}] + 0.1\Sigma$
$1_e$	$1.0[0.9L_{  } + 0.1L_{\perp}]$
$2_e$	$1.0[0.9L_{  } + 0.1L_{\perp}]$
$3_e$	[a] $1.0[0.3L_{  } + 0.7L_{\perp}]$ ; [b] $1.0[0.9L_{  } + 0.1L_{\perp}]$
$4_e$	$1.0[0.9L_{  } + 0.1L_{\perp}]$

<sup>a</sup> Here,  $0.8[0.9L_{||} + 0.1L_{\perp}] + 0.2\Sigma$  means 80% L character (comprised of 90%  $L_{||}$  and 10%  $L_{\perp}$ ), and 20%  $\Sigma$  character. Some peaks have two different types of characters, as specified by [a] or [b] because each DOS peak is made up of many single-particle energy levels.

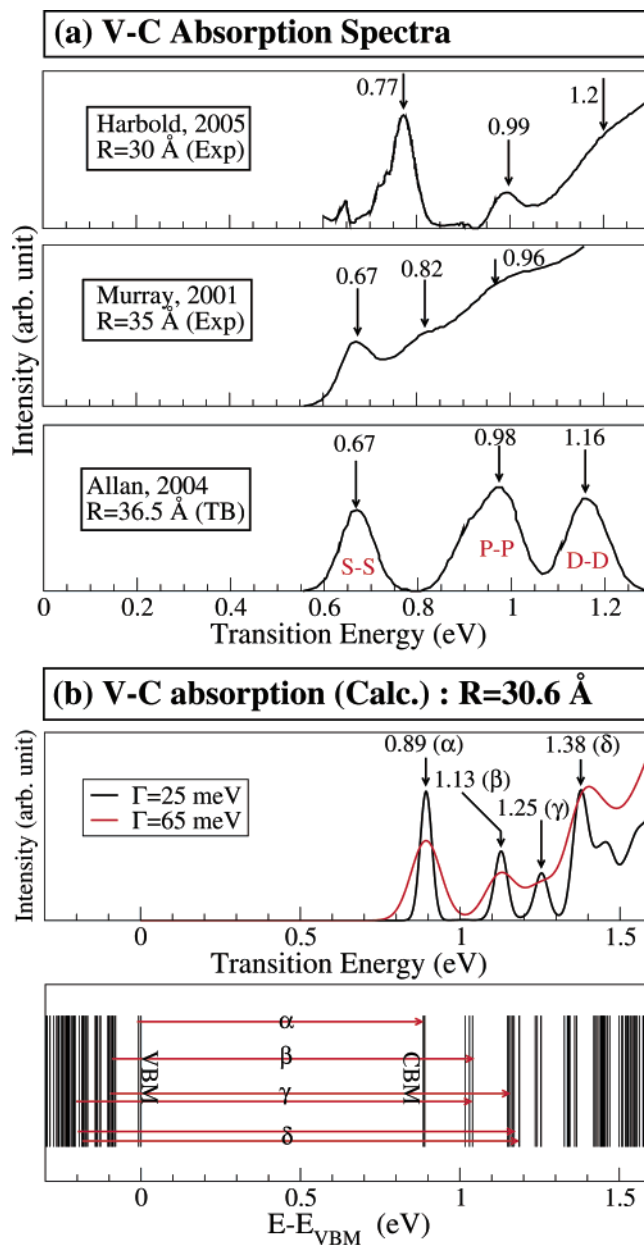
**Valence-to-Valence (V-V) Intraband Transitions.** Figure 5a shows the experimental intraband differential absorption spectrum measured by Wehrenberger et al.<sup>4</sup> for 36- $\text{\AA}$ -radius PbSe quantum dots. The authors<sup>4</sup> reported an induced absorption feature centered around 0.174 eV ( $=1400 \text{ cm}^{-1}$ ). This feature consists of a narrow dip superimposed on a broad peak. They interpreted the dip<sup>30</sup> as an extrinsic effect arising from absorption by molecular species moving in and out of the film while charging, concluding that there is but one intrinsic absorption peak due to the dot. Our results disagree with this interpretation in that we find two distinct intrinsic intraband absorption peaks arising from two split groups of levels by the anisotropic effective mass (without the interference from molecular species causing the dip). Note further that the measured intraband absorption peak could be obscured by the size dispersion of the dots of average radius  $R = 36 \text{ \AA}$ , different from our dot size  $R = 30.6 \text{ \AA}$ . Two absorption peaks were also predicted in ref 14, in agreement with our result.

Figure 5b shows our calculated valence energy levels of a 30.6- $\text{\AA}$ -radius dot and the corresponding V-V absorption spectrum broadened with a Gaussian of width  $\Gamma = 25 \text{ meV}$  at a temperature of 12 K. At such a low temperature, only the four lowest dot levels are thermally populated. Table 4 summarizes all of the transition peak assignments (first and second columns) relevant for V-V absorption. The calculated spectrum displays two well-defined absorption peaks:  $\alpha$  being  $1_h \rightarrow 2_h^{(1)}$  [a] at 0.10 eV and  $\beta$  being  $1_h \rightarrow 3_h^{(2)}$  [b] at 0.23 eV for  $R = 30.6 \text{ \AA}$ . Transition  $\alpha$  is mostly  $L_{||} \rightarrow L_{||}$ , whereas  $\beta$  is primarily  $L_{||} \rightarrow L_{\perp}$  (Table 3). Note that the intraband V-V absorption is dominated by direct L-to-L transitions, whereas states having large  $\Sigma$  character do not contribute to intraband transitions. However, the spectrum for the dot of  $R = 15.3 \text{ \AA}$  shows more diverse features because of the relatively sparse states. It has two major peaks at transition energies 0.136 and 0.292 eV. Comparison with tunneling spectra<sup>15</sup> in Table 2 shows a good agreement for the large dot:  $\alpha$  calculated (measured) being 0.090 eV (0.095 eV) and  $\beta$  calculated (measured) being 0.227 eV (0.224 eV);  $2_h^{(1)}-3_h^{(2)}$  calculated (measured) being 0.137 eV (0.129 eV).



**Figure 5.** Experimental intraband (a) valence-to-valence (V-V) (c) conduction-to-conduction (C-C) absorption spectra of 36-Å-radius dots reported by Wehrenberg et al.<sup>4</sup> are compared with our calculated single-particle intraband spectra for (b) V-V and (d) C-C transitions of 30.6-Å-radius dots with  $\Gamma = 25$  meV at 12 K. Shown in the bottom panels of b and d are single-particle energy levels with arrows specifying states involved in transitions that make up absorption spectral peaks shown in the upper panels.

**Conduction-to-Conduction (C-C) Intraband Transitions.** Figure 5c shows the experimental C-C intraband



**Figure 6.** (a) Measured and calculated interband valence-to-conduction (V-C) absorption spectra from refs 8, 6, and 14, (b) our calculated absorption transitions for the 30.6-Å-radius dot with linewidths  $\Gamma = 25, 65$  meV; in the lower panel of b, single-particle energy levels are shown with allowed transitions specified by arrows, and in the upper panel are shown their corresponding absorption spectral peaks with transition energy values.

absorption of Wehrenberger et al.<sup>4</sup> for the dot of  $R = 36$  Å. The authors<sup>4</sup> assigned the peak centered around 0.186 eV ( $= 1500 \text{ cm}^{-1}$ ) to the  $1S_e - 1P_e$  transition. The TB results by Allan et al.<sup>14</sup> showed one broad peak around 0.129 eV for  $R = 36.5$  Å. However, the electron effective mass anisotropy at the L point was not fully incorporated in the TB fit. Our calculation produces two distinct peaks for the 30.6 Å dot with a Gaussian broadening of  $\Gamma = 25$  meV, as shown in Figure 5d. The first absorption peak,  $\alpha$ , at transition energy 0.145 eV, originates from a transition  $1_e \rightarrow 2_e$  ( $L_{||} \rightarrow L_{||}$ ), whereas the second peak,  $\beta$ , at 0.268 eV, stems from  $1_e \rightarrow 3_e$  [ $a$ ] ( $L_{||} \rightarrow L_{\perp}$ ), as shown in Table 4.

**Table 4.** Transitions Involved in Intra- and Interband Absorption for the  $R = 30.6 \text{ \AA}$  Dot, their Transition Character, and their Transition Energy<sup>a</sup>

$\alpha$ (V-V)	$\beta$ (V-V)	$\alpha$ (C-C)	$\beta$ (C-C)	$\alpha$ (V-C)	$\beta$ (V-C)	$\gamma$ (V-C)	$\delta$ (V-C)
$1_h \rightarrow 2_h^{(1)}[a]$	$1_h \rightarrow 3_h^{(2)}$	$1_e \rightarrow 2_e$	$1_e \rightarrow 3_e[a]$	$1_h \rightarrow 1_e$	$2_h^{(1)}[a] \rightarrow 2_e$	$2_h^{(1)}[a] \rightarrow 3_e [b]; 3_h^{(2)}[a] \rightarrow 2_e$	$3_h^{(1)}[a] \rightarrow 3_e; 3_h^{(2)}[a] \rightarrow 3_e[a]$
$L_{  } \rightarrow L_{  }$	$L_{  } \rightarrow L_{\perp}$	$L_{  } \rightarrow L_{  }$	$L_{  } \rightarrow L_{\perp}$	$L_{  } \rightarrow L_{  }$	$L_{  } \rightarrow L_{  }$	$L_{  } \rightarrow L_{\perp}; L_{\perp} \rightarrow L_{  }$	$L_{  } \rightarrow L_{  }; L_{\perp} \rightarrow L_{\perp}$
0.100 eV	0.230 eV	0.145 eV	0.268 eV	0.890 eV	1.130 eV	1.250 eV	1.380 eV

<sup>a</sup>  $\alpha$ ,  $\beta$ , and  $\gamma$  are the absorption peak labels specified in Figures 5 and 6. All symbols refer to Table 3.

**Table 5.** Interband Absorption Peak-to-Peak Energy Difference Extracted from Optical Absorption Spectra<sup>8,16</sup> and Our Calculation:  $\epsilon_{\beta} - \epsilon_{\alpha}$  or  $\epsilon_{\delta} - \epsilon_{\beta}$  Represent the Energy Difference between Peaks  $\beta$  and  $\alpha$  or between  $\delta$  and  $\beta$  in Interband V-C Spectra (All Energies are in Electronvolts)

radius ( $\text{\AA}$ )	$\epsilon_{\beta} - \epsilon_{\alpha}$	$\epsilon_{\delta} - \epsilon_{\beta}$
15.3; <sup>a</sup> 30.6 <sup>a</sup>	0.42; 0.24	0.33; 0.25
30 <sup>c</sup>	0.21	0.22
30; <sup>b</sup> 36 <sup>c</sup>	0.20; 0.15	
15.3; <sup>c</sup> 27.5 <sup>c</sup>	0.42; 0.22	

<sup>a</sup> Presently calculated values. <sup>b</sup> Optical absorption, ref 8. <sup>c</sup> Optical absorption, ref 16.

The transition energies of  $\alpha$  and  $\beta$  can also be estimated by the DOS peak separations corresponding to the transition assignments in Table 2:  $\alpha \approx 1_e - 2_e = 0.144 \text{ eV}$  (measured: 0.145 eV);  $\beta \approx 1_e - 3_e = 0.278 \text{ eV}$  (measured: 0.272 eV);  $2_e - 3_e = 0.134 \text{ eV}$  (measured: 0.127 eV);  $3_e - 4_e = 0.080 \text{ eV}$  (measured: 0.056 eV). Similar to the intraband V-V absorption, we find that the level splitting due to anisotropic electron effective mass plays a crucial role in C-C transitions, that is, two absorptive transitions to  $L_{||}$  and  $L_{\perp}$  final states split by the L-point anisotropy.

**Valence-to-Conduction (V-C) Interband Transitions.** Experimental<sup>6,8</sup> and calculated<sup>14</sup> V-C spectra are shown in Figure 6a. Figure 6b displays our calculated single-particle energy levels and their corresponding interband V-C absorption spectrum. Using a broadening of  $\Gamma = 25 \text{ meV}$ , we resolve four distinct peaks ( $\alpha$ ,  $\beta$ ,  $\gamma$ , and  $\delta$ ) each of which is associated with transitions having relatively large oscillator strengths. However, applying a  $\Gamma = 65 \text{ meV}$  broadening washes out the  $\gamma$  peak and resolves three well-defined peaks ( $\alpha$ ,  $\beta$ ,  $\delta$ ) in accordance with experimentally observed spectra. Our calculated absorption peak separations for both  $R = 15.3 \text{ \AA}$  and  $R = 30.6 \text{ \AA}$  are in excellent agreement with the experimental values, as shown in Table 5.

The origin of the second absorption peak has generated much controversy in the literature. Our atomistic calculations provide a different interpretation of the experimental spectra than previous calculations.<sup>5,12-14</sup> Table 4 shows our identification of the absorption peaks. We see that peak  $\alpha$  is  $1_h \rightarrow 1_e$ , that is,  $L_{||} \rightarrow L_{||}$ . Peak  $\beta$  is also  $L_{||} \rightarrow L_{||}$  due to  $2_h^{(1)}[a] \rightarrow 2_e$ . In other words, peaks  $\alpha$  and  $\beta$  are associated with the symmetric transition  $L_{||} \rightarrow L_{||}$  giving relatively larger oscillator strengths. The  $\gamma$  peak originates from two distinct types of anisotropically asymmetric transitions with relatively small oscillator strengths:  $L_{||} \rightarrow L_{\perp}$  and  $L_{\perp} \rightarrow L_{||}$ . This accounts for their relatively smaller oscillator strengths. Peak  $\delta$  is made up of two symmetric transitions,  $L_{||} \rightarrow L_{||}$  and  $L_{\perp} \rightarrow L_{\perp}$ .

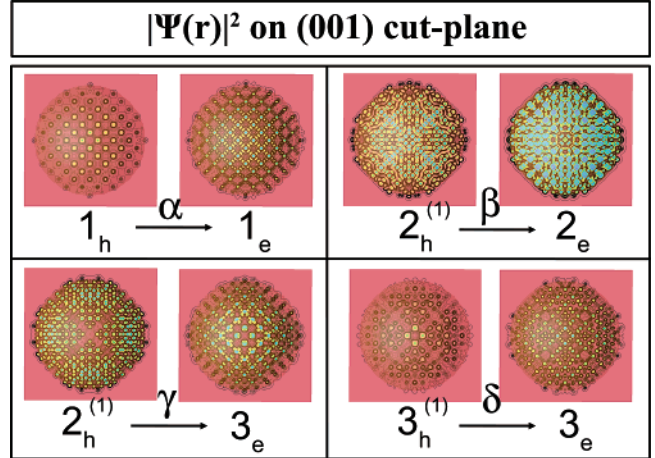


**Figure 7.**  $|\psi_i(\mathbf{r})|^2$ 's depicting a set of interband transitions,  $\alpha$ ,  $\beta$ ,  $\gamma$ ,  $\delta$ , each corresponding to  $h1 \rightarrow e1$ ,  $h8 \rightarrow e8$ ,  $h18 \rightarrow e11$ , and  $h48 \rightarrow e17$  among a set of single-particle states belonging to DOS peaks for  $R = 30.6 \text{ \AA}$ : The contours represent  $|\psi_i(\mathbf{r})|^2$ 's on the (001) cut-plane dissecting the dot with their intensities increasing from red to blue.

To better characterize the interband transitions, we show in Figure 4 the areas in the Brillouin zone from which the initial and final states derive. Furthermore, Figure 7 shows the real-space atomistic wavefunctions corresponding to the four calculated absorption peaks. Unlike the simple effective mass approximation results cited in the current literature,<sup>3,4,10,11,16,21</sup> our calculations indicate that there is no way to assign pure orbital angular momenta of envelope functions because of intervalley coupling and state-mixing from different parts of the Brillouin zone. Nevertheless, our wavefunction analysis in both real (Figure 7) and reciprocal (Figure 4) space suggests that transition  $\alpha$  involves approximate S-like hole and electron states; transition  $\beta$  is associated with P-like hole and electron states; transition  $\gamma$  is characteristic of asymmetric transitions having mixed P- and D-like states; finally, transition  $\delta$  is due to symmetric transitions ( $L_{||}^h \rightarrow L_{||}^e$  and  $L_{\perp}^h \rightarrow L_{\perp}^e$ ), characteristic of a number of heavily mixed P- and D-like states.

Our interpretation of the second transition as  $1P_h \rightarrow 1P_e$  interband optical transition is in apparent contradiction with the observation of Wehrenberg et al.<sup>4</sup> who found that, when electrons (undetermined numbers<sup>4</sup>) are progressively injected into the dot, bleaching of the second optical transition begins before bleaching of the first optical transition is complete. This observation suggested to the authors that both transitions involve the same set of final states ( $S_e$ ) whose occupation blocks additional optical transitions into these states (Pauli blocking). However, the bleaching of both first and second transitions upon charging could be consistent

with having different final states ( $S_e$  for the first and  $P_e$  for the second, respectively). This is related to the fact that the experiment of ref 4 pertains to a highly charged dot, not to a neutral dot. Such high charging will repel the electron and attract the hole resulting from an additional photoexcited pair, thus separating it spatially and reducing its intensity, particularly if the charges are trapped at or near the dot surface.<sup>31</sup> This is true both for  $S_h-S_e$  and  $P_h-P_e$  photoexcited pairs. Thus, Coulomb-induced intensity attenuation (and not just Pauli blocking) can explain the bleaching of the second transition. Therefore, the final state of the first and second transitions need not be the same, as deduced by Wehrenberg et al.<sup>4</sup>

Clear evidence that the second transition is  $P_h \rightarrow P_e$ , not  $P_h \rightarrow S_e$ , was given by recent tunneling spectroscopy measurements.<sup>15</sup> The authors first measured the single-particle hole and electron states (viz. Figure 3), finding the energetic distance for the  $P_h \rightarrow P_e$  and  $P_h \rightarrow S_e$  pairs. Comparing these energy differences to the absorption spectra, they found that the second absorption peak (corrected by e-h Coulomb effects) corresponds to the  $P_h \rightarrow P_e$  energy difference from tunneling, whereas the  $P_h \rightarrow S_e$  energy difference from tunneling is a few hundreds of a millielectronvolt lower than the second absorption peak. Clearly, the second absorption peak is not due to the forbidden  $S-P$  excitation.

In summary, referring to the questions i-iii raised in the introduction, we find that (i) The band-edge states of PbSe nanocrystals evolve from the extensively split L-like VBM and CBM and partially from the  $\Sigma$ -like bands. The L-L splitting is caused by intervalley coupling, valence-conduction interband mixing, L-valley anisotropy and finite confining potential. (ii) The splitting of the L valley into  $L_{||}$  and  $L_{\perp}$  causes the isotropic  $P_h \rightarrow P_e$  transition to split into  $L_{||}^h \rightarrow L_{||}^e$  and  $L_{\perp}^h \rightarrow L_{\perp}^e$ . This gives rise to the  $\beta$  peak corresponding to the observed second peak and the  $\gamma$  peak that may be difficult to observe because of nanocrystal size dispersion. Thus, the second absorption peak is the allowed  $P_h \rightarrow P_e$  transition, not the forbidden  $S_h \rightarrow P_e$  (or  $P_h \rightarrow S_e$ ) as suggested previously. The observed third peak, corresponding to the calculated  $\delta$  peak, arises from two different types of symmetric transitions,  $L_{||}^h \rightarrow L_{||}^e$  and  $L_{\perp}^h \rightarrow L_{\perp}^e$  of a number of heavily mixed P- and D-like single-particle states. (iii) The hole levels are significantly more closely spaced than the electron levels (Figure 1) on account of L-point intervalley mixing,  $\Sigma$ -point contribution, and a finite confinement barrier, a finding that invalidates previous suggestions of a mirror-like symmetry between electrons and holes.

**Acknowledgment.** We thank P. Guyot-Sionnest for illuminating discussions of his work,<sup>30</sup> and P. Liljeroth for allowing us to use his data in ref 15. This work was funded by the U.S. Department of Energy, Office of Science, Basic Energy Science, Materials Sciences and Engineering, under Contract No. DE-AC36-99GO10337 to NREL.

## References

- (1) Wei, S. H.; Zunger, A. *Phys. Rev. B* **1997**, *55*, 13605.
- (2) Lifshitz, E.; Bashouti, M.; Kloper, V.; Kigel, A.; Eisen, M. S.; Berger, S. *Nano Lett.* **2003**, *3*, 857.
- (3) Wehrenberg, B. L.; Wang, C.; Guyot-Sionnest, P. *J. Phys. Chem. B* **2002**, *106*, 10634.
- (4) Wehrenberg, B. L.; Guyot-Sionnest, P. *J. Am. Chem. Soc.* **2003**, *125*, 7807.
- (5) Kang, I.; Wise, F. W. *J. Opt. Soc. Am. B* **1997**, *14*, 1632.
- (6) Murray, C. B.; Sun, S.; Gaschler, W.; Doyle, H.; Betley, T. A.; Kagan, C. R. *IBM J. Res. Dev.* **2001**, *45*, 47.
- (7) Du, H.; Chen, C.; Krishnan, R.; Krauss, T. D.; Harbold, J. M.; Wise, F. W.; Thomas, M. G.; Silcox, J. *Nano Lett.* **2002**, *2*, 1321.
- (8) Harbold, J. M.; Du, H.; Krauss, T. D.; Cho, K.-S.; Murray, C. B.; Wise, F. W. *Phys. Rev. B* **2005**, *72*, 195312.
- (9) Hens, Z.; Vanmaekelbergh, D.; Kooij, E. S.; Wormeester, H.; Allan, G.; Delerue, C. *Phys. Rev. Lett.* **2004**, *92*, 026808.
- (10) Schaller, R. D.; Klimov, V. I. *Phys. Rev. Lett.* **2004**, *92*, 1886601.
- (11) Ellingson, R. J.; Beard, M. C.; Johnson, J. C.; Yu, P.; Micic, O. I.; Nozik, A. J.; Shabaev, A.; Efros, A. L. *Nano Lett.* **2005**, *5*, 865.
- (12) (a) Andreev, A. D.; Kolobkova, E. V.; Lipovskii, A. A. *J. Appl. Phys.* **2000**, *88*, 750. (b) Andreev, A. D.; Lipovskii, A. A. *Phys. Rev. B* **1999**, *59*, 15402.
- (13) Tudury, G. E.; Marquezini, M. V.; Ferreira, L. G.; Barbosa, L. C.; Cesar, C. L. *Phys. Rev. B* **2000**, *62*, 7357.
- (14) Allan, G.; Delerue, C. *Phys. Rev. B* **2004**, *70*, 245321.
- (15) Liljeroth, P.; van Emmichoven, P. A. Z.; Hickey, S. G.; Weller, H.; Grandidier, B.; Allan, G.; Vanmaekelbergh, D. *Phys. Rev. Lett.* **2005**, *95*, 086801.
- (16) Schaller, R. D.; Pietryga, J. M.; Goupalov, S. V.; Petruska, M. A.; Ivanov, S. A.; Klimov, V. I. *Phys. Rev. Lett.* **2005**, *95*, 196401.
- (17) (a) Volkov, B. A.; Pankratov, O. A.; Sazonov, A. V. *Sov. Phys. Semiconductors-USSR* **1982**, *16*, 1112-1118. (b) Volkov, B. A.; Pankratov, O. A. *Sov. Phys., JETP* **1978**, *48*, 687 calculated the band structure in a 12-parameter p orbital only tight-binding approach finding qualitatively correct band structure, which, however, fails to quantitatively reproduce most of the quantities of Table 1.
- (18) Reboredo, F. A.; Zunger, A. *Phys. Rev. B* **2000**, *62*, R2275.
- (19) Landolt; Börtstein *Group III Condensed Matter*; Springer-Verlag: Berlin, 1998; Vol. 41.
- (20) Mitchell, D. L.; Wallis, R. F. *Phys. Rev.* **1966**, *151*, 581.
- (21) Klimov, V. I.; McBranch, D. W. *Phys. Rev. Lett.* **1998**, *80*, 4028.
- (22) Wang, L. W.; Zunger, A. *Phys. Rev. B* **1995**, *51*, 17398.
- (23) Kim, K.; Kent, P. R. C.; Zunger, A.; Geller, C. B. *Phys. Rev. B* **2002**, *66*, 045208.
- (24) Califano, M.; Franceschetti, A.; Zunger, A. *Nano Lett.* **2005**, *5*, 2360.
- (25) Wang, L. W.; Zunger, A. *J. Chem. Phys.* **1994**, *100*, 2394.
- (26) Wang, L. W.; Bellaiche, L.; Wei, S. H.; Zunger, A. *Phys. Rev. Lett.* **1998**, *80*, 4725.
- (27) The measured band gaps in ref 11 are smaller than those measured in refs 3 and 8. For example, in ref 11  $E_g = 0.680$  eV for a 30.6 Å dot, whereas in ref 3  $E_g = 0.865$  eV for a 29-Å-radius dot and  $E_g = 0.688$  eV for a 35.5-Å-radius dot, and in ref 8  $E_g = 0.769$  eV for a 30-Å-radius dot.
- (28) Franceschetti, A.; An, J. M.; Zunger, A. *Nano Lett.* **2006**, *6*, 2191.
- (29) Franceschetti, A.; Zunger, A. *Phys. Rev. B* **2000**, *62*, 2614.
- (30) Private communication with P. Guyot-Sionnest about his work in ref 4.
- (31) Wang, L.-W. *J. Phys. Chem. B* **2001**, *105*, 2360.
- (32) Franceschetti, A.; Fu, H.; Wang, L. W.; Zunger, A. *Phys. Rev. B* **1999**, *60*, 1819.
- (33) Albanesi, E. A.; Okoye, C. M. I.; Rodriguez, C. O.; y Blanca, E. L. P.; Petukhov, A. G. *Phys. Rev. B* **2000**, *61*, 16589.
- (34) Hinkel, V.; Haak, H.; Mariani, C.; Sorba, L.; Horn, K. *Phys. Rev. B* **1989**, *40*, 5549.
- (35) Kinoshita, J.; Glosser, R. *Phys. Lett. A* **1974**, *48*, 393.

NL061684X